REVIEW SUMMARY

BIOIMAGING

Vibrational spectroscopic imaging of living systems: An emerging platform for biology and medicine

Ji-Xin Cheng* and X. Sunney Xie*

BACKGROUND: Biomolecules can serve as natural labels for microscopy by measuring their molecular vibration spectra in living cells and tissues. However, the transition from spectroscopy of molecules in cuvettes to spectroscopic imaging of living systems requires more than putting spectrometers on microscopes. A series of technical challenges must be addressed, such as delivery of light beams for sample excitation and scattering of signals, which limit the probe depth of spectroscopic imaging. There are also trade-offs in how large a spectral window can be measured at a pixel (the amount of chemical information) in a given amount of time (the recording speed).

ADVANCES: Several technical advances made by different groups have pushed the boundary of the vibrational spectroscopic imaging field in terms of spectral acquisition speed, detection sensitivity, spatial resolution, and penetration depth. Specifically, coherent Raman scattering microscopy has emerged as a high-speed vibrational imaging platform. Single-frequency coherent anti-Stokes Raman scattering (CARS) and stimulated Raman scattering (SRS) microscopes have reached a video-rate imaging speed. Multiplex CARS by broadband excitation has reached a speed of 3.5 ms per pixel; multiplex SRS covering a window of 200 wave numbers has reached a speed of 32 µs per pixel.

The marriage of high-speed coherent Raman microscopy and Raman-sensitive tags of large cross sections has enabled real-time imaging of small molecules at micromolar concentration. Nanoscale vibrational imaging has been demonstrated by integration of atomic force microscopy and vibrational spectroscopy. Vibrational imaging of deep tissue has been enabled by acoustic detection of overtone transitions or optical detection of diffuse photons. Biological applications of CARS and SRS microscopy have generated new insights into myelin biology, lipid droplet biology, intracellular drug delivery, and single-cell metabolism. Meanwhile, clinical applications of vibrational spectroscopic imaging are enabling molecule-based diagnosis of cancer and heart disease without the need for any exogenous contrast agent. Examples include intravascular vibrational photoacoustic imaging of lipid-laden plaques and spatially offset Raman spectroscopic detection of cancer margins.

OUTLOOK: There remain two central challenges facing the field. One is to increase the detection sensitivity of vibrational microscopy to micromolar or even nanomolar levels, so that low-concentration biomolecules in a living system can be mapped. The other is to increase the vibrational imaging depth to tens of centimeters for noninvasive molecule-based medical diagnosis.

With continuous developments, high-resolution, high-speed vibrational microscopy will cultivate unexpected discoveries in cell biology. The findings may lead to the development of new therapies for currently incurable diseases. Meanwhile, with further improvement of penetration depth and progressive reduction of instrument size, vibrational spectroscopic imaging devices are expected to become fundamental clinical tools for disease diagnosis and therapy effectiveness evaluation. ∎
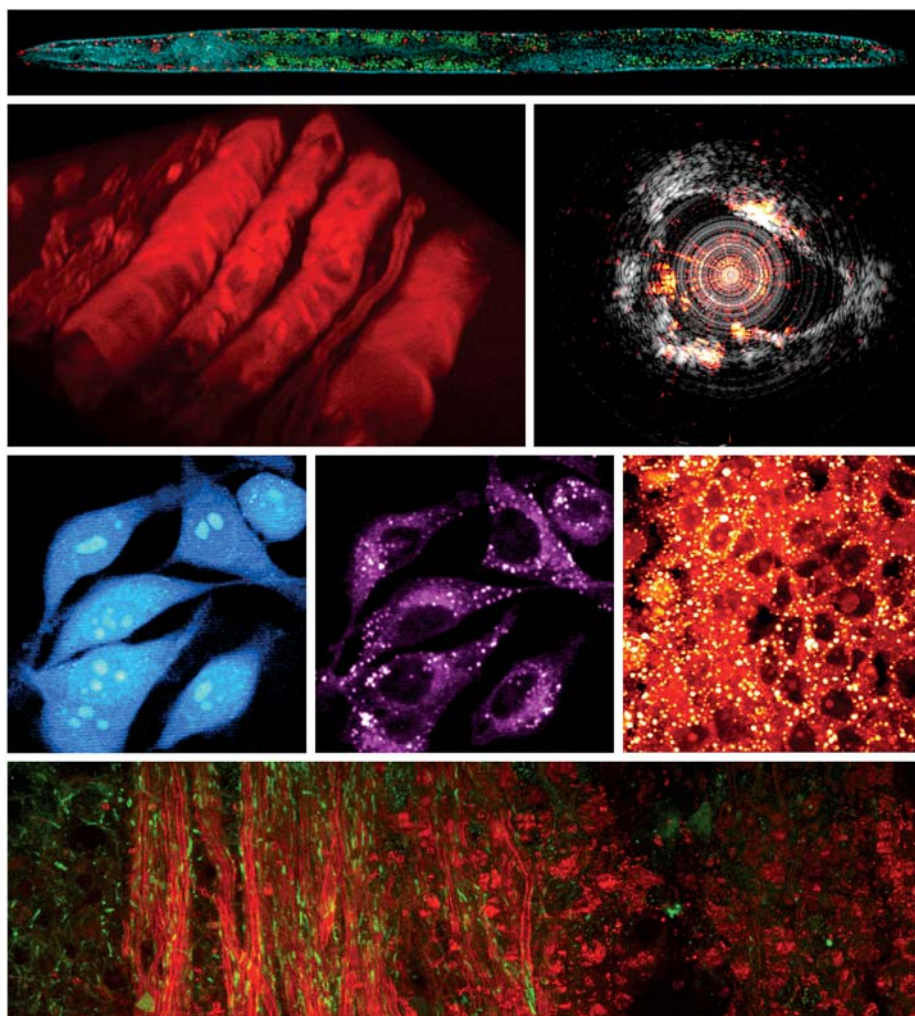
Molecular fingerprints for biology and medicine through imaging. Recent efforts focused on pushing the fundamental limits of vibrational spectroscopic imaging in terms of spectral acquisition speed, detection sensitivity, spatial resolution, and penetration depth. The resulting platforms are enabling transformative applications in functional analysis of single living cells and noninvasive diagnosis of human diseases with biomarker sensitivity.

BIOIMAGING

Vibrational spectroscopic imaging of living systems: An emerging platform for biology and medicine

Ji-Xin Cheng[1]* and X. Sunney Xie[2]*

Vibrational spectroscopy has been extensively applied to the study of molecules in gas phase, in condensed phase, and at interfaces. The transition from spectroscopy to spectroscopic imaging of living systems, which allows the spectrum of biomolecules to act as natural contrast, is opening new opportunities to reveal cellular machinery and to enable molecule-based diagnosis. Such a transition, however, involves more than a simple combination of spectrometry and microscopy. We review recent efforts that have pushed the boundary of the vibrational spectroscopic imaging field in terms of spectral acquisition speed, detection sensitivity, spatial resolution, and imaging depth. We further highlight recent applications in functional analysis of single cells and in label-free detection of diseases.

A century ago, stains developed by Golgi allowed Ramón y Cajal to picture neuronal cells in the central nervous system. More recently, the discovery of green fluorescent proteins facilitated the imaging of protein dynamics in living cells and animals. The development of superresolution fluorescence microscopy has further enabled close examination of cellular structures at the nanometer scale. Despite such advances, the labeling approach has various limitations: (i) Labels may perturb the function of a biological molecule or structure; (ii) the labeling approach offers limited capacity of discovery because it is only applicable to known species; (iii) delivery of labels to a target could be difficult, especially under in vivo conditions; and (iv) the potential toxicity often prevents the use of labels in human subjects.

The emerging field of in vivo vibrational spectroscopic imaging delivers a way to circumvent such barriers. The concept of vibrational spectroscopic imaging can be explained by the children's book *Where's Waldo*. In this book, by simple pattern recognition (his distinctive cap), children locate Waldo in an image of crowds without a need for labels. Similarly, molecules can be recognized by their distinctive signature, or "fingerprint," produced by quantized vibrations of chemical bonds. Fingerprint vibrational spectra of molecules in a single cell can be recorded by infrared (IR) or Raman spectroscopy. Nonetheless, a cell is not a bag of molecules, but rather a spatially and temporally organized dynamic system. If a finger-print spectrum could be recorded at every pixel with sufficient speed and a multivariate analysis performed on the resulting data set, a given "Waldo" molecule could be located and monitored in real time in a living system, thereby gaining insight into its function.

The transition from spectroscopy to spectroscopic imaging of living systems, however, cannot be accomplished simply by combining a spectrometer and a microscope. A series of technical difficulties need to be addressed: Can we increase the speed of spectral acquisition to the microsecond scale in order to capture the dynamics in a living cell? Can we achieve enough sensitivity to detect target molecules in a tissue environment (whose propensity for scattering light degrades images) without harming the cells? Can we have superior resolution to enable imaging of biological structures at the nanoscale? Finally, can we detect a spectrum from a centimeter-deep tissue for in vivo diagnosis? Advances toward overcoming these technical difficulties are discussed below.

Molecular fingerprint vibration spectra can be recorded through measurements of linear IR absorption or inelastic Raman scattering. Fourier-transform IR microscopy has enabled chemical imaging of histological slices [reviewed in (*1*)]. Live-cell imaging applications of IR spectroscopy are, however, hampered by the strong water absorption of IR light and also by the low spatial resolution given the long wavelength (a few micrometers) of IR light. Raman spectroscopy, which uses shorter-wavelength visible light for excitation, has been extensively used for analysis of cells and tissues [reviewed in (*2*)]. Feld, Puppels, Popp, and others have demonstrated broad biomedical applications of Raman spectroscopy. A Raman microscope, first reported in the 1970s, is now commercially available and has reached a speed of milliseconds per pixel. Nonetheless, because of the extremely small cross section of spontaneous Raman scattering, the bioimaging speed of a state-of-the-art Raman microscope is limited to tens of minutes per frame (*3*), insufficient for capturing the dynamics (e.g., movement of organelles) inside living cells.

Coherent Raman scattering (CRS) microscopy (*4*) is an emerging technique that overcomes the frame rate limitation of spontaneous Raman microscopy. In most CRS imaging experiments, two excitation fields are used, denoted as pump (ω_p) and Stokes (ω_s). When the beating frequency ($\omega_p - \omega_s$) between the pump and Stokes fields is resonant with a Raman-active molecular vibration, four major CRS processes occur simultaneously, namely coherent anti-Stokes Raman scattering (CARS) at a new frequency of ($\omega_p - \omega_s$) + ω_p, coherent Stokes Raman scattering at a new frequency of $\omega_s - (\omega_p - \omega_s)$, stimulated Raman gain (SRG) at ω_s, and stimulated Raman loss (SRL) at ω_p. CARS is a parametric phenomenon in which the input and output photons exchange energy while the quantum state of the molecule is left unchanged. As a vibrationally enhanced four-wave mixing process, the CARS signal is generated at a new frequency apart from input beams and is accompanied by a nonresonant signal caused by electronic contributions to the four-wave mixing process. SRG and SRL belong to the process of stimulated Raman scattering (SRS), in which the Stokes beam experiences a gain in intensity and the pump beam experiences an intensity loss. SRS is a dissipative process in which energy corresponding to the beating frequency ($\omega_p - \omega_s$) of input photons is transferred to the molecule for vibrational excitation. The SRS signal appears at the same wavelengths as the excitation fields and is commonly extracted through a lock-in amplifier. Figure 1 shows the schematics of spontaneous Raman scattering, CARS, and SRS.

CARS as a third-order nonlinear process was documented in 1965 by Terhune and Maker at the Ford Motor Company (*5*). Coherent anti-Stokes Raman spectroscopy (*6*) has been widely used for monitoring chemical reaction dynamics and remains a powerful tool for combustion analysis. The CARS microscope was reported in 1982 by Duncan *et al.* using a two-dimensional (2D) imaging device (*7*). In 1999, Zumbusch *et al.* demonstrated 3D CARS imaging of live cells by raster-scanning two collinearly overlapped and tightly focused femtosecond pulse excitation beams (*8*). This work triggered the development of modern CARS microscopy. By spectrally focusing the excitation energy on a single Raman band by means of picosecond pulses, Cheng *et al.* demonstrated CARS imaging of cells in the fingerprint vibration region (*9*) and further developed a high-speed laser-scanning CARS microscope for visualization of cell mitosis and apoptosis (*10*). Epi-detected (i.e., backward-detected) CARS was developed to minimize the detection of nonresonant signals (*11*) and was later used for imaging live animals at video rate (*12*). A Green's function model was developed to interpret the radiation pattern of CARS from a 3D object and thereby explain the contrast mechanism (*13*). At the same time, multiplex CARS

[1]Weldon School of Biomedical Engineering and Department of Chemistry, Purdue University, West Lafayette, IN 47907, USA. [2]Department of Chemistry and Chemical Biology, Harvard University, Cambridge, MA 02138, USA.
*Corresponding author. E-mail: jcheng@purdue.edu (J.-X.C.); xie@chemistry.harvard.edu (X.S.X.)

Input   **Output**
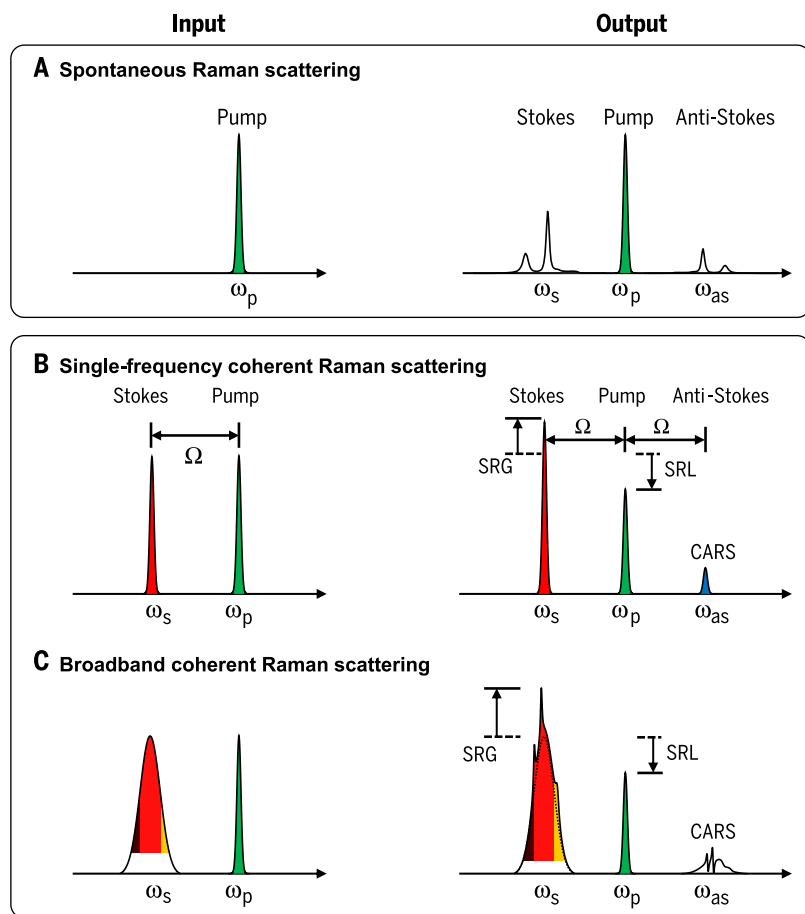
Fig. 1. Spontaneous versus coherent Raman scattering process. (**A**) A narrowband pump laser generates spontaneous Raman scattering. (**B**) Two narrowband lasers generate single-frequency coherent Raman scattering. (**C**) A narrowband laser and a broadband laser simultaneously excite multiple Raman transitions. SRG, stimulated Raman gain; SRL, stimulated Raman loss; CARS, coherent anti-Stokes Raman scattering. ω_p, ω_s, and ω_{as} denote the frequencies of the pump, Stokes beam, and anti-Stokes beam, respectively; Ω is the fundamental.

microscopy was developed for spectroscopic imaging (*14*, *15*). The strong signal contributed by C-H stretching vibrations has led to the application of CARS microscopy in lipid biology [reviewed in (*16*)].

The SRS phenomenon was reported in 1962 (*17*). Owyoung and co-workers developed SRS spectroscopy with continuous-wave lasers in the 1970s (*18*). Ploetz *et al.* demonstrated SRS imaging of polymer beads with a broadband, low–repetition rate laser in 2007 (*19*). In 2008, the Xie group reported high-speed, high-sensitivity single-frequency SRS imaging by megahertz modulation of a picosecond laser and modulation transfer to the other laser (*20*), and this work was quickly followed by reports from the Volkmer group, the Ozeki group, and others (*21–25*). The SRS signal can be extracted at the optical modulation frequency by either a lock-in amplifier (*20–25*) or a tuned amplifier (*26*). SRS is free of nonresonant background and provides spectral profiles that are nearly identical to spontaneous Raman spectroscopy. Moreover, the SRS intensity is linearly dependent on molecular concentration. These fea-

tures render SRS microscopy a robust and quantitative method for chemical imaging [reviewed in (*27*, *28*)].

The vibrational signal can also be detected indirectly with acoustic signatures generated by optical absorption. The photoacoustic effect, first documented by Bell in 1880 (*29*), offers an elegant route toward deep-tissue molecular imaging. When photons are absorbed by a molecule, part of the absorbed energy is converted into heat. The local heating results in a thermal expansion that creates a transient pressure wave detectable by an ultrasonic transducer. The time of flight of the photoacoustic signal carries the information about the location of the absorbers, and thus the distribution of the molecular absorbers can be mapped through image reconstruction. Photoacoustic tomography and microscopy have found wide biomedical applications based on the electronic absorption of hemoglobin [reviewed in (*30*, *31*)].

In an effort to overcome the limited imaging depth of CRS microscopy, which is on the scale of 100 μm, two photoacoustic vibrational imaging

platforms—one based on overtone absorption (*32*) and the other on SRS (*33*)—have been demonstrated. In the SRS-based platform, the energy difference of the pump and Stokes beam, $\hbar(\omega_p - \omega_s)$ (where $\hbar$ is Planck's constant divided by 2π), is absorbed by the interacted molecules (*34*) to generate acoustic waves (*33*, *35*). The SRS-based platform relies mostly on ballistic photons, which limits its potential for deep-tissue photoacoustic imaging. In overtone-based photoacoustic imaging (*36*), pulsed near-IR light induces overtone vibrational absorption. Through the heat dissipation process, such vibrational absorption is converted into a detectable transient acoustic wave. Unlike the strong mid-IR absorption by water in living organisms, the overtone vibrational bands are located in the near-IR region, where spectral windows of minimal water absorption exist for deep-tissue, bond-selective imaging (*32*). Moreover, unlike the SRS process, both diffuse and ballistic photons contribute to overtone absorption equally. This platform has led to the development of a high-speed intravascular vibrational photoacoustic (IVPA) catheter for label-free imaging of lipid-laden plaques (*37*) and vibration-based photoacoustic tomography (*38*) for label-free detection of breast cancer margin (*39*) and nerves (*40*). Besides the photoacoustic detection scheme, vibrational imaging of deep tissues has been pursued via spatially offset Raman spectroscopy (*41*), Raman tomography (*42*), and near-IR diffuse optical tomography (*43*).

Below, we discuss strategies contributed by different research groups that have pushed the boundary of the vibrational spectroscopic imaging field in terms of acquisition speed, detection sensitivity, spatial resolution, and imaging depth. We also highlight important applications enabled by these technical advances.

Pushing the limit of imaging speed

The imaging speed in spontaneous Raman, CARS, and SRS microscopy is dictated by the signal-to-noise ratio (SNR) at certain pixel dwell times. In all of these microscopic techniques, three major sources of noise are typically present: photon shot noise, laser intensity excess noise, and detector Johnson noise. Generally, Raman spectroscopy has a very low level of signal photons and the Johnson noise is the SNR-limiting factor. Thus, it takes milliseconds to seconds to record a Raman spectrum, and minutes to acquire a Raman image. CARS microscopy gains speed through coherent addition of the radiation fields, which renders the signal large and highly directional (*13*). The laser beams in CARS microscopy are usually not modulated. Thus, the laser intensity excess noise is transferred to the signal and becomes the SNR-limiting factor. In highly concentrated conditions, such as imaging lipid bodies by C-H stretch vibrations, a pixel dwell time of <1 μs is achieved. Experimentally, video-rate CARS imaging of skin lipids in living mice has been reported (*12*).

SRS microscopy gains speed through signal amplification by the presence of a local oscillator at the detection wavelength. SRS imaging usually involves intensity modulation of one laser and extraction of modulated signals from the other.

The shot noise in SRS microscopy is much greater than that in CARS. Meanwhile, because of the modulation and demodulation at MHz frequency, contribution from the excess laser noise is substantially reduced. Thus, the shot noise limit can be reached at a pixel dwell time of 100 ns, as demonstrated by video-rate single-frequency SRS imaging (44).

The above discussion considers CARS or SRS resonance with a single vibrational frequency. Without providing spectral information, this configuration is only applicable to mapping known species in a specimen. Hyperspectral CARS and SRS microscopy has been developed by sweeping the laser wavelength. A spectral resolution better than 10 cm^{-1} has been reached by femtosecond pulse-shaping technology (45, 46). With these methods, it takes seconds to minutes to record an entire stack of images for reconstruction. Such speed is not sufficient to capture dynamics in a living system without spectral distortion.

Many research groups are developing multiplex CARS and SRS microscopy, in which a spectrum is instantaneously recorded at each pixel. First reported in 2002, multiplex CARS microscopy and microspectroscopy use a broadband and a narrowband beam to produce a CARS spectrum recorded by a spectrometer (14, 15). Later, it was realized that the nonresonant background can be used as a local oscillator to enhance the resonant signal in multiplex CARS imaging (47). Two methods, maximum entropy (48) and Kramers-Kronig transformation (49), were adopted to extract the Raman spectrum from the CARS signal. Alternatively, with the addition of a third beam, interferometric CARS was developed to produce Raman spectral data at each pixel (50). Broadband CARS covering the entire Raman window was developed by using supercontinuum laser sources (51). Using this method, spectral acquisition on the order of a few milliseconds per pixel was recently achieved by Cicerone and co-workers (51).

In a further advance toward multiplex SRS detection, Fu et al. demonstrated multicolor imaging by modulation multiplexing and parallel detection of three spectral channels (52). Marx et al. compared various multichannel detectors that can be potentially used for SRS microscopy (53). Rock et al. reported the recovery of an SRS spectrum from a complementary metal-oxide semiconductor array with 20-ms integration time (54). Seto et al. developed a multiplex SRS microscope through multichannel lock-in detection, with a moderate detection sensitivity of 10^{-4} modulation (55). With a 32-channel resonant amplifier array, Liao et al. demonstrated lock-in free multiplex SRS imaging, within a spectral window defined by the femtosecond pulse, with pixel dwell time of 32 μs and detection sensitivity of 10^{-6} modulation (56). By spatial frequency multiplexing of a femtosecond pulse, Liao et al. further demonstrated microsecond-scale vibrational spectroscopic imaging by single photodiode detection of diffuse photons (57).

Along with efforts to improve instrumentation, various multivariate analysis methods were adopted to decompose the spectroscopic image into chemical maps of major components. For samples of known compositions, least-squares fitting provides a solid and rapid means to generate concentration maps (58). For samples with limited prior knowledge, principal components analysis (59), k-means clustering (60), independent components analysis (45), or spectral phasor analysis (61) can identify the major components in a CARS or SRS image. Concentration maps of these major components can be produced by further multivariate curve resolution analysis (62). Similar methods were developed by the Cicerone group (63) and the Langbein group (64).

At present, taking a CARS spectrum of the full window (3000 cm^{-1}) requires a few milliseconds per pixel. SRS spectra covering a window of hundreds of wave numbers can be recorded in microseconds, whereas single-frequency CARS or SRS signals can be acquired in nanoseconds.

Pushing the limit of detection sensitivity

With picosecond pulse excitation, single-frequency CARS microscopy has reached the detection sensitivity of ~1 million C-H bonds in a lipid membrane (65), which corresponds to millimolar molecular concentration in a femtoliter excitation volume. For weaker Raman bands, the CARS signal is often buried in a large nonresonant background contributed by the medium. Various advanced detection schemes have been developed to suppress the nonresonant background, including polarization-sensitive detection, time-resolved detection, interferometric CARS, and frequency modulation, but the complex configurations of these schemes have limited their application [reviewed in (66)]. Epi-detected CARS (11), which avoids the forward-propagating nonresonant signal contributed by the solvent, allows quantitative imaging of domains in a single supported lipid layer (67). Recently, the Potma group demonstrated surface-enhanced CARS detection of a single molecule located in a gold dumbbell by time-resolved measurement (68).

Under the shot noise–limited condition, the detection sensitivities of SRS and CARS are comparable (21). By excitation with a time-lens laser source synchronized with a femtosecond pulse, a hyperspectral SRS imaging sensitivity of 5×10^{-6} modulation depth for C-H vibrations in dimethyl sulfoxide (DMSO) was reached at a pixel dwell time of 2 μs, which corresponds to 19 mM DMSO in water (69). In hyperspectral SRS imaging, denoising (70) and subsequent multivariate data analysis allowed separation of spectroscopic signal from the unwanted cross-phase modulation, which improved the SNR in final chemical maps. For single-frequency SRS microscopy, advanced-phase or spectral modulation schemes were developed to remove the non-Raman background [reviewed in (28)].

Raman tags with large scattering cross sections offer an effective approach to improve molecular selectivity and boost detection sensitivity. Relative to fluorescent labels, Raman tags have smaller volumes and thus provide a promising way of imaging small biomolecules without perturbing their intracellular functions. Raman tags use vibrational signatures of the carbon-deuterium

(C-D) bond, the cyano bond (C≡N), or the alkyne bond (C≡C), which are spectrally isolated from the endogenous Raman bands. The alkyne tag has allowed direct Raman visualization of DNA synthesis and mobile small molecules in living cells (71, 72), at a speed of 50 min per frame of 127 × 127 pixels. CRS microscopy was deployed for faster imaging of C-D–labeled fatty acids (23, 73), amino acids (74), and drugs (75) in living cells. More recently, SRS imaging of alkyne-tagged molecules has been reported (76, 77), with detection sensitivity at the level of 200 μm.

Pushing the limit of spatial resolution

As nonlinear optical processes, CARS and SRS offer submicrometer lateral spatial resolution and an axial sectioning capability of ~1 μm. In order to study subcellular structures, partition of chemicals within an organelle, and cell functional activity, it is desirable to have higher imaging resolution. The use of two laser fields for signal generation opens opportunities to exceed the optical diffraction limit in CARS and SRS microscopy. Superresolution CARS imaging that achieved 130-nm lateral resolution for imaging nanostructured materials has been reported (78). By using ground-state population depletion, superior resolution was demonstrated through saturated transient absorption microscopy (79) and has been proposed for SRS microscopy (80). In this modality (79), a donut-shaped saturation beam was used to deplete the ground-state population, which restricted the pump-probe volume to the very center of the focus. Experimental demonstration of super-resolution SRS imaging is expected in the near future.

Near-field scanning optical microscopy has achieved imaging resolution well below 100 nm and has been deployed for nanoscale vibrational imaging. By combining atomic force microscopy and IR absorption spectroscopy, Keilmann and co-workers used a near-field probe tip (rather than laser beam focusing) to obtain surface-enhanced contrast in vibrational absorption of chemical compounds (81). Here, a silicon cantilevered probing tip was metallized with a 100-nm layer of gold to achieve a diffraction-limited imaging resolution and enhanced IR absorption around the tip's apex. Application of this nanoscale spectroscopic absorption signal to life science has not yet been reported.

Pushing the limit of imaging depth

As the number of ballistic photons rapidly decreases with depth in a turbid tissue, current approaches of deep-tissue vibrational imaging exploit the interaction between diffuse photons and molecules to extract vibrational spectroscopic information. These methods are based on the detection of (i) overtone vibrational signal via near-IR diffuse optical tomography, (ii) vibrationally scattered photons through spatially offset Raman spectroscopy or Raman tomography, or (iii) the ultrasound signal induced by overtone vibrational absorption.

In near-IR diffuse optical tomography, photons interact with molecular overtone and
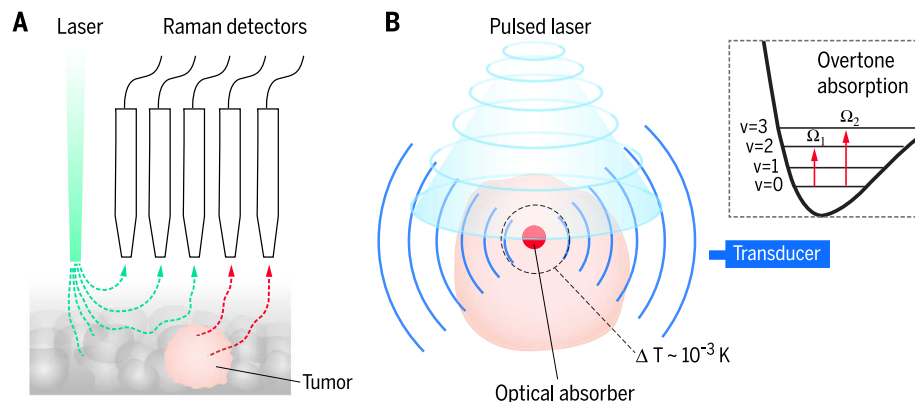
Fig. 2. Modalities for vibrational imaging of deep tissue. (**A**) Spatially offset Raman spectroscopy entails a spatial offset between the incident laser and the Raman signal probe, which allows detection of objects such as a tumor deep under the tissue surface. The green and red dotted lines indicate incident and Raman photons, respectively. (**B**) Vibration-based photoacoustic tomography is a modality in which a pulsed laser induces molecular overtone transitions inside a tissue. Subsequent relaxation of vibrational energy into heat generates acoustic waves detectable by an ultrasound transducer. Ω_1 and Ω_2 are the first and second overtone transition frequencies.

combinational vibrational transitions, which are allowed by the anharmonicity of chemical bond vibration (*82*). The transition frequency of an overtone band is described by $\Omega = \Omega_0 n - \chi\Omega_0(n + n^2)$, where Ω_0 is the frequency of a fundamental vibration, χ is the anharmonicity, and $n = 2, 3, \dots$ represents the first overtone, second overtone, and so on. By modeling photon diffusion in turbid tissue, molecule-specific information can be obtained through approximately extracting absorption from the elastic scattering of photons (*83*). Spatial distribution of the molecule can be tomographically reconstructed by solving the "inverse problem" in a diffusion equation.

Unlike SRS, spontaneous Raman scattering is a linear inelastic scattering process and is less dependent on tight focusing for signal generation. Thus, diffuse photons that travel deep into the tissue could contribute substantially to a Raman spectrum. An intuitive way of extracting molecular information from different depths is to use ultrafast temporal gating (*84*, *85*), which measures the time-of-flight Raman signal generated from diffused photons. On the basis of these studies, Matousek and co-workers demonstrated spatially offset Raman spectroscopy as an effective and relatively simple method to obtain molecular information from deep tissue (*41*) (Fig. 2A). In this method, when collecting a Raman signal from a surface position that is laterally offset from the position of excitation, a larger portion of backscattered Raman photons from a deeper layer is detected rather than those from an upper layer (*41*). With modeling of light propagation and multivariate analysis of the Raman spectrum, molecule-specific information at a tissue depth of a few millimeters can be extracted (*86–89*). Raman tomography (*90*, *91*), developed by Morris and Pogue, works in a manner similar to diffuse optical imaging, where the propagation of the inelastically scattered photons is described by diffusion equations. By detecting the

diffusely propagated Raman-scattered photons in a 360° plane, the spatial distribution of molecules at depths greater than 1 cm can be reconstructed (*92*, *93*).

Excited by near-IR pulsed lasers, the molecular vibrational energy is quickly relaxed into heat and converted into mechanical energy via tissue expansion and retraction. The generated pressure waves can then be detected with an acoustic transducer (Fig. 2B). This overtone-based photoacoustic imaging method has been used for mapping objects that are rich in C-H bonds (*32*, *36*, *94*). The second and first overtones of C-H stretch vibration—located at ~1210 nm and ~1730 nm, respectively—were chosen by taking advantage of their relatively large absorption coefficients (*36*, *95–97*). As the wavelength increases, water absorption starts to become a factor and attenuates the light that can arrive to deep tissue. Thus, selection of the spectral window is critical to maximize the contrast of C-H bonds over O-H bonds while maintaining a certain imaging depth (*98*). Providing a stronger photoacoustic signal, the first overtone of C-H bonds is favorable in the applications where millimeter-scale penetration depth is needed. When dealing with applications requiring a penetration depth greater than a few millimeters, the second overtone becomes a better choice (*96–98*).

Shedding light on cellular machinery

CRS microscopy provides submicrometer resolution and can resolve intracellular organelles, which is especially important for single-cell studies. Small biomolecules including amino acids, nucleic acids, lipids, and carbohydrates play essential roles in cell proliferation and function. Because of their small sizes, their activity inside cells would be considerably changed by the bulky fluorescent labels. Applications of CARS and SRS microscopy have contributed to new understanding of lipid droplet biology, myelin biology, cell metabolism, cell cycle,

drug delivery, and tissue organization, as summarized below. Although we focus on mammalian cells and tissues here, we note that SRS microscopy has also been applied to botanical science (*99*, *100*).

In a label-free manner, CARS and SRS microscopy have been widely used to study two important organelles—lipid droplets and the myelin sheath—that generate strong signals from C-H stretching vibrations. In 2004, Nan *et al.* reported CARS imaging of the process of adipogenesis in live 3T3-L1 cells (*101*). In 2007, Hellerer *et al.* reported CARS imaging of fat storage in live *Caenorhabditis elegans* (*102*). These studies were followed by multiple studies on lipid droplet biology, including trafficking (*103*), lipolysis (*104*), growth (Fig. 3A) (*105*), and dietary fat absorption through the small intestine (*16*). Without interference with non-resonant background, SRS microscopy provides a new way to study lipid metabolism in model organisms. Wang *et al.* coupled SRS microscopy and RNA interference screening to identify genetic regulators of fat storage in *C. elegans* (*106*). Dou *et al.* found active transport of lipid droplets in early fruit fly embryos by femtosecond pulse–stimulated Raman-loss imaging (*107*). Using hyperspectral SRS imaging of fingerprint Raman bands, Wang *et al.* resolved fat droplets, cholesterol-rich lysosomes, and lipid oxidation in wild-type and mutant worms (*108*). Multiplex SRS microscopy allowed separation of fat droplets from protein-rich organelles, using their spectroscopic signatures of the CH_2 bending mode (*56*). By integrating single-frequency CARS microscopy with Raman microspectroscopy for compositional analysis (*109*) (Fig. 3B), Yue *et al.* reported that lipid droplets in human patient prostate cancer cells are rich in cholesteryl ester (*110*). This finding presents a new way to treat aggressive cancers by abrogating the activity of cholesterol esterification.

The myelin sheath, a multilamellar membrane surrounding the axon, is responsible for rapid propagation of action potentials in a saltatory manner. Myelin sheath degradation leads to serious disorders such as multiple sclerosis. The myelin sheath is abundant in lipids and produces a strong CARS signal that allows label-free imaging of myelin in its natural tissue environment (*111*, *112*). The 3D sectioning capability of CARS allowed visualization of detailed myelin structure, such as the node of Ranvier (*113*) (Fig. 3C). Different groups have used CARS microscopy to characterize myelin degradation and regeneration under different conditions of diseases and/or white matter injury (*111*, *113*, *114*). CARS has been further used to longitudinally monitor demyelination and remyelination in an injured spinal cord in vivo (*113*). More recently, Hu *et al.* demonstrated in vivo SRS imaging of single myelin sheaths in early-stage tadpoles (*115*). These studies collectively demonstrate a CRS-based platform for mechanistic study of myelin diseases.

Both CARS and SRS microscopy have enabled dynamic imaging of metabolic conversions in single living cells. By hyperspectral SRS imaging of fingerprint bands and multivariate analysis, Wang *et al.* monitored multiple metabolites in

small intestine cells of live *C. elegans* (*108*) (Fig. 4A). Liao *et al.* observed the conversion of retinol into retinoic acids in cancer cells (*56*). Isotope substitution has been used to selectively monitor the fate of specific metabolites. The C-D bond produces Raman peaks around 2100 cm^{-1}, spectrally isolated from endogenous Raman modes. SRS imaging of deuterated fatty acids administered to live cells revealed that oleic acids facilitate the conversion of palmitic acid into neutral lipid stored in lipid droplets (*23*). Min and co-workers used deuterated amino acids as substrates for mapping protein synthesis by SRS microscopy (*74*) (Fig. 4B). They further extended this work to monitor the process of protein degradation using ^{13}C-labeled phenylalanine (*116*). By using deuterated glucose, Li *et al.* demonstrated direct visualization of de novo lipogenesis in pancreatic cancer cells, which occurs at a much lower rate in immortalized normal pancreatic epithelial cells (*117*). A similar strategy has been used to monitor choline metabolism at the single-cell level (*118*). The alkyne-based Raman tags open a new avenue to monitor DNA and RNA synthesis and drug distribution in living cells (*76*, *77*). By synthesis of phenol-diyne cholesterol, Lee *et al.* reported SRS imaging of cholesterol storage in *C. elegans* (Fig. 4C) and lysosomal storage of cholesterol in a cellular model of Niemann-Pick type C disease, with a detection sensitivity of 31 μM phenol-diyne cholesterol (*119*).

High-speed CRS microscopy has enabled chemical imaging of cell mitosis and apoptosis. In 2002, CARS microscopy was used to detect cell apoptosis according to signals from the plasma membrane and nucleus (*10*). Such capability has been amplified by selective imaging of lipids and proteins based on signals from CH$_2$ and CH$_3$ vibrations (*120*). Recently, SRS microscopy allowed real-time monitoring of the cell cycle based on selective imaging of DNA, using its distinctive signature in the high–wave number C-H vibration region (*121*) (Fig. 4D).

CRS microscopy is becoming a powerful tool for mapping spatial and temporal dynamics of drug molecules for which fluorescent labeling would alter their physical properties. A number of groups applied CARS and SRS to map the distribution and follow the release of active pharmaceutical ingredients (Fig. 4E) (*122*–*125*). Guy and co-workers monitored molecular diffusion into the human nail (*126*). Fu *et al.* applied hyperspectral SRS microscopy to visualize drug distribution inside cells using fingerprint Raman bands (*127*).

CRS microscopy has further enabled chemical imaging of tissues with 3D sectioning capability. Three major advances have been made: (i) CARS-based multimodal nonlinear optical microscopy has been developed to visualize multiple species in a tissue environment (*128*); (ii) histology-mimicking two-color contrast has been achieved by combined imaging of CH$_2$ vibration for lipids and CH$_3$ vibration for proteins (*129*); and (iii) hyperspectral CARS and SRS microscopy has allowed chemical imaging of multiple molecules using spectrally overlapped fingerprint Raman bands (*49*, *64*, *108*). These studies laid the groundwork for the development of mobile imaging devices that would be useful for in vivo diagnosis applications in clinical settings.

Moving into the clinic

High-speed, high-resolution vibrational spectroscopic imaging is expected to affect the current paradigm of medical practice by enabling molecule-based diagnosis without the need for any contrast agent. Generally, CRS microscopy provides submicrometer spatial resolution, together with an imaging depth and a field of view both on the order of 100 μm. On the basis of these characteristics, CARS and SRS microscopy are considered to be suitable for in vivo imaging of skin or exposed tissue.

Toward this direction, a few groups have reported preliminary results in developing CARS and SRS microendoscopy (*130*–*132*). For clinical applications, the integration of CARS with multiphoton fluorescence and second-harmonic generation modalities allowed microscopic examination of lipids, endogenous fluorophores, and collagen fibers in human skin (*133*). Koenig *et al.* demonstrated clinical CARS imaging to provide label-free in vivo skin biopsy (*134*, *135*) (Fig. 5A). Potma and co-workers applied SRS microscopy to identify squamous cell carcinoma in human skin (*136*) (Fig. 5B). Ji *et al.* applied two-color SRS microscopy to map CH$_2$ and CH$_3$ vibrations at Raman shifts of 2845 and 2930 cm^{-1} (*137*). Using a linear recombination method, they extracted maps of lipids and proteins that reflected the proper distribution of cellular bodies and extracellular structures. This two-color SRS imaging method was also applied in vivo in mice to reveal brain tumor margins that were not detectable under standard operative conditions (*137*) (Fig. 5C). We note that fiber-optic Raman spectroscopy has been used for intraoperative brain tumor detection during surgery on a human patient (*138*). Relative to single-point Raman spectroscopy, SRS microscopy provides visual information that resembles hematoxylin and eosin–based histology (*110*, *129*).

Various deep-tissue vibrational imaging methods are opening new ways for minimally invasive diagnosis of human diseases. By photoacoustic detection of C-H bonds' overtone transition, several groups are developing IVPA catheters for visualization of lipid deposition inside the blood vessel wall, with an imaging depth of a few millimeters (*32*, *95*, *139*). Multivariate analysis of the overtone spectrum has been applied to extract chemically specific information. Differentiation of CH$_2$-rich fat and CH$_3$-rich collagen in atherosclerotic arteries was achieved by vibrational photoacoustic imaging through the distinctive spectral profiles of CH$_2$ and CH$_3$ groups (*36*, *96*, *97*). Clinical translation of IVPA imaging has been hampered by the lack of suitable high–repetition rate lasers for excitation of the first overtone of C-H bonds at 1730 nm or the second overtone around 1200 nm. By shifting the wavelength from a 1064-nm YAG laser via the SRS process, a Raman laser offers a solution

Fig. 3. Biological applications of coherent anti-Stokes Raman scattering (CARS) microscopy. (**A**) Real-time CARS imaging reveals neutral lipid depletion in 3T3-L1 adipocytes. Left: 0 min; right: 2.5 hours. Scale bars, 10 μm. (**B**) Integrating coherent Raman imaging with spontaneous Raman spectroscopy. Left: CARS image of lipid bodies in a living 3T3-L1 cell. Right: Raman spectrum of a single lipid droplet (marked with a cross in the CARS image) reveals its chemical composition. Scale bar, 20 μm. (**C**) Left and center: Ex vivo CARS imaging reveals chemically induced myelin sheath swelling in a spinal cord tissue. Right: In vivo CARS image of a node of Ranvier inside the white matter of a rat spinal cord. Scale bars, 10 μm.
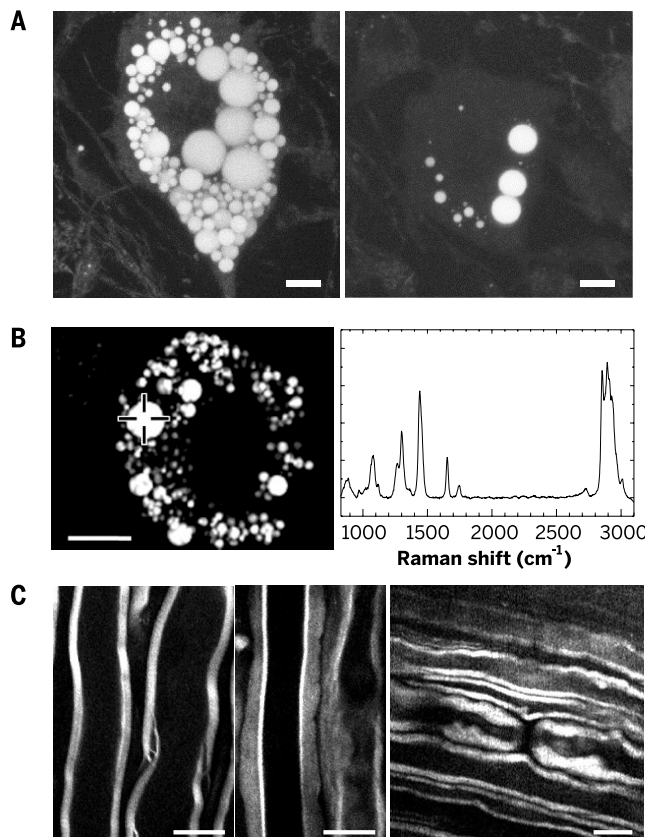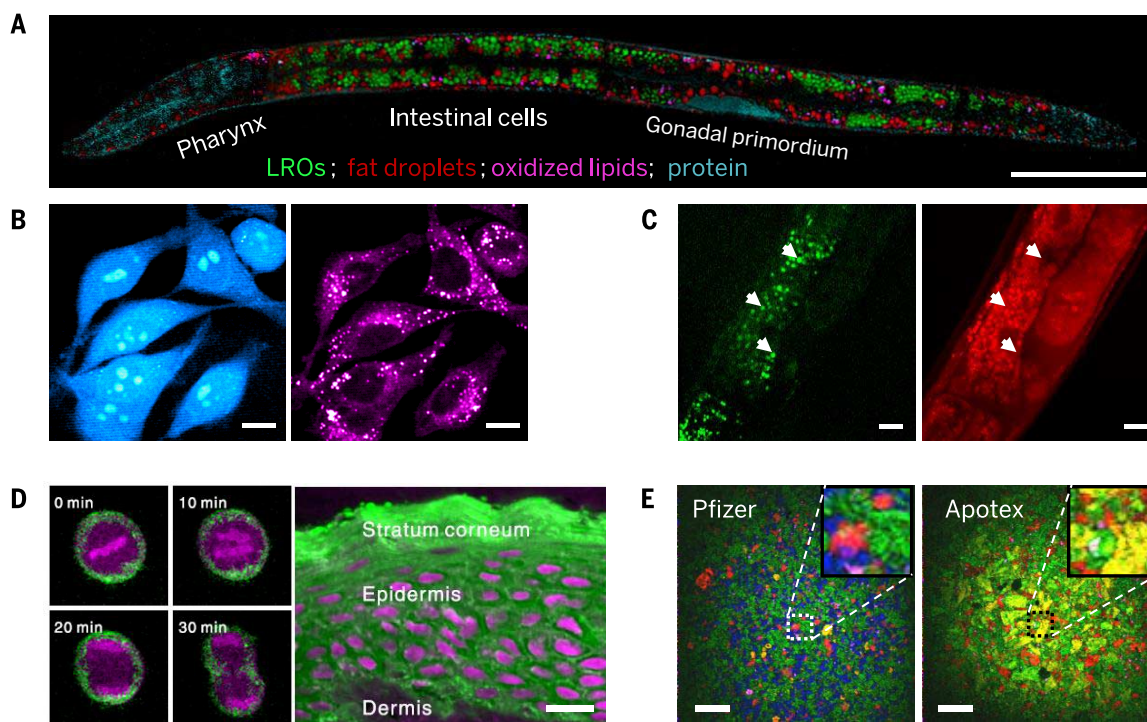
Fig. 4. Biological applications of stimulated Raman scattering (SRS) microscopy. (**A**) Chemical maps of intracellular compartments in *C. elegans* generated by hyperspectral SRS imaging and multivariate curve resolution analysis. The green, red, magenta, and cyan colors represent lysosome-related organelles (LROs), neutral fat droplets, oxidized lipids, and proteins, respectively, in the body of a *daf-2* mutant. Scale bar, 50 μm. (**B**) SRS imaging of live HeLa cells using signals from C-D vibration at 2133 cm^{-1} (left) and C-H vibration at 2845 cm^{-1} (right). The C-D signal shows newly synthesized proteins by metabolic incorporation of a deuterium-labeled set of amino acids. Scale bars, 10 μm. (**C**) SRS imaging of phenyl-diyne cholesterol in live *C. elegans*. Left: SRS image at C≡C vibrational mode at 2247 cm^{-1} reveals a distinct cholesterol store in the worm. Right: SRS image at 2885 cm^{-1} reveals C-H–rich fat stores. Scale bars, 10 μm. (**D**) Left: Time-lapse SRS images of DNA (magenta) and lipids (green) in a HeLa cell undergoing cell division. Right: SRS images of DNA (magenta) and lipids (green) in a normal human skin tissue section. Scale bar, 20 μm. (**E**) Large-area SRS images of drug tablets from Pfizer (left) and Apotex (right). Green, blue, red, yellow/orange, and magenta colors represent micro-crystalline cellulose, dibasic calcium phosphate anhydrous, amlodipine besylate (drug), sodium starch glycolate, and magnesium stearate, respectively. Scale bars, 200 μm.

for vibrational photoacoustic imaging of lipids (*140*). By constructing a 2-kHz Raman laser at 1197 nm, Wang *et al.* demonstrated high-speed IVPA imaging of lipid-laden plaque in an intact artery at a speed of 1 frame per second (Fig. 5D) (*37*). Development of kilohertz lasers at 1730 nm is important for in vivo IVPA imaging.

In the tomography domain, Tromberg and co-workers deployed molecular vibration–based diffuse optical imaging for quantitation of water and lipid content within turbid tissue (*141*, *142*). In the optical window typically from 600 to 1000 nm, lipid has a peak at ~930 nm, which is assigned to the third overtone of the CH$_2$ stretching mode, and water has a peak at ~980 nm, which is assigned to the combination of symmetric and asymmetric stretching modes of the O–H bond (*82*). The quantification of water and lipid according to their absorption signature has been used to determine the malignancy of breast tissue in vivo, where an imaging depth of a few centimeters has been achieved (*143*). With high chemical specificity, both spatially offset Raman spectroscopy and Raman tomography have shown promise as tools for breast cancer margin assessment and bone characterization (*91*, *93*, *144–146*). Coupling overtone absorption of lipids with elec-tronic absorption contrast from hemoglobin, photoacoustic tomography was applied to breast tumor margin assessment (Fig. 5E) and peripheral nerve visualization (*39*, *40*).

Outlook

Through integration with advances in other fields, new technical breakthroughs are expected that will further increase detection sensitivity, acquisition speed, imaging depth, and spatial resolution. The current detectable concentration of CARS or SRS microscopy is above 1.0 mM for endogenous molecules. Such sensitivity prohibits wide biological applications of coherent Raman microscopy, because most biomolecules inside cells are at a nanomolar to micromolar level. Because CARS and SRS microscopy have reached the shot noise limit, a possible way of improving the detection sensitivity could be through non-optical detection. For example, through force measurement of SRS-induced chemical bond vibration, single-molecule sensitivity has been reported (*147*). Extension of this method to biological imaging remains to be demonstrated. If single-molecule detection sensitivity is reached for vibrational imaging of living cells, then we can, in principle, reach nanoscale spatial resolution as in fluorescence microscopy. Along the direction of high-speed imaging, with parallel modulation schemes, frequency-multiplexed SRS could potentially reach a speed of 1000 frames per second to enable monitoring of very fast processes. Along the direction of deeper imaging, integrating vibrational spectroscopy with techniques that enable active focusing of light through a turbid tissue, such as time reversal of ultrasound-coded light (*148*, *149*), might allow deep-tissue vibrational imaging for in vivo diagnosis.

For single-cell functional analysis, we expect high-speed vibrational spectroscopic imaging to be applied in studies of cell activities. Examples include monitoring the propagation of action potential using intrinsic vibrational signal from the neuronal membrane, following the transport and release of neurotransmitters, and measuring changes of protein conformation inside smooth muscle cells under mechanical stress.

Finally, we believe that cooperation among physicists, engineers, entrepreneurs, and clinicians is important for clinical translation of in vivo vibrational imaging technologies. We expect advances in the reduction of technology cost and instrument size. Progress in ultrafast fiber laser technology, although not covered in this review,
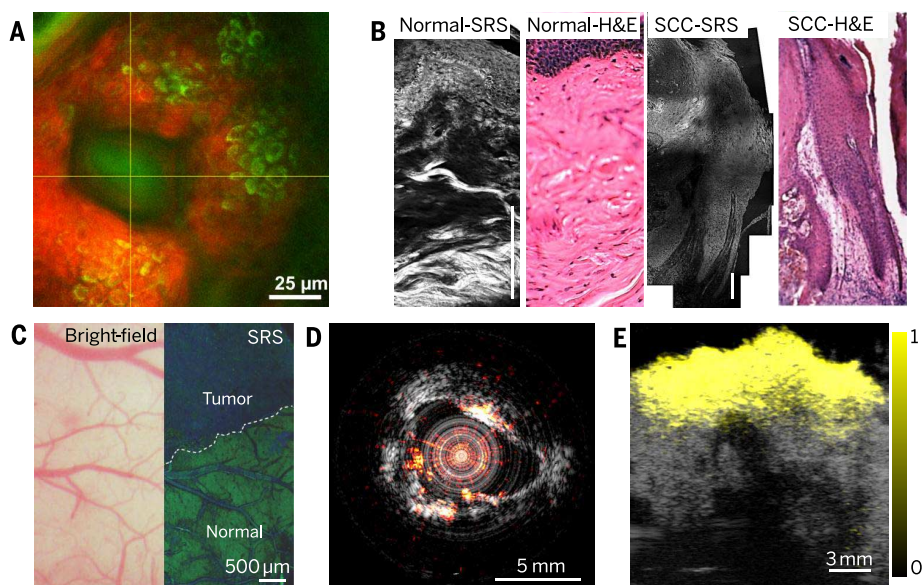
Fig. 5. Clinical applications of vibrational spectroscopic imaging. (**A**) In vivo cellular imaging shows structures of an excretory duct of the sweat gland from healthy human skin. Green, two-photon excitation fluorescence; red, CARS. (**B**) From left to right: Stimulated Raman scattering (SRS) image of healthy human skin; hematoxylin and eosin (H&E)–stained specimen of an adjacent healthy skin section; SRS image of superficial squamous cell carcinoma (SCC); H&E-stained specimen of an adjacent SCC section. Scale bars, 100 μm. (**C**) Bright-field (left) and SRS (right) images of a margin between a brain tumor and normal brain tissue in a human glioblastoma multiforme xenografted mouse. The contrast in the SRS image provides label-free detection of the tumor margin. (**D**) Intravascular photoacoustic (fire color) and ultrasound (gray) imaging of an atherosclerotic artery. The photoacoustic signal shows the distribution of lipids deposited inside the arterial wall. (**E**) Photoacoustic (yellow) and ultrasound (gray) tomographic imaging of a human breast tumor tissue section. The photoacoustic signal arising from C-H overtone absorption demonstrates the lipid-rich tumor margin.

promises to enable mobile CARS and SRS imaging systems. Invenio Imaging Inc. has produced a fiber laser–based commercial system for SRS imaging (*150*). Likewise, nanosecond lasers with kilohertz repetition rates have shown promise for high-speed intravascular imaging of lipid-laden plaques (*37*). These efforts are expected to convert vibrational spectroscopic imaging platforms into fundamental clinical tools for in vivo detection of residual disease or longitudinal evaluation of therapy effectiveness.

REFERENCES AND NOTES

1. R. Bhargava, Infrared spectroscopic imaging: The next generation. *Appl. Spectrosc.* **66**, 1091–1120 (2012). doi: 10.1366/12-06801; pmid: 23031693
2. Z. Movasaghi, S. Rehman, I. U. Rehman, Raman spectroscopy of biological tissues. *Appl. Spectrosc. Rev.* **42**, 493–541 (2007). doi: 10.1080/05704920701551530
3. A. F. Palonpon et al., Raman and SERS microscopy for molecular imaging of live cells. *Nat. Protoc.* **8**, 677–692 (2013). doi: 10.1038/nprot.2013.030; pmid: 23471112
4. J.-X. Cheng, X. S. Xie, *Coherent Raman Scattering Microscopy* (CRC Press, Boca Raton, FL, 2013).
5. R. W. Terhune, P. D. Maker, C. M. Savage, Measurements of nonlinear light scattering. *Phys. Rev. Lett.* **14**, 681–684 (1965). doi: 10.1103/PhysRevLett.14.681
6. R. Begley, A. Harvey, R. L. Byer, Coherent anti-Stokes Raman spectroscopy. *Appl. Phys. Lett.* **25**, 387 (1974). doi: 10.1063/1.1655519
7. M. D. Duncan, J. Reintjes, T. J. Manuccia, Scanning coherent anti-Stokes Raman microscope. *Opt. Lett.* **7**, 350–352 (1982). doi: 10.1364/OL.7.000350; pmid: 19714017
8. A. Zumbusch, G. R. Holtom, X. S. Xie, Three-dimensional vibrational imaging by coherent anti-Stokes Raman scattering. *Phys. Rev. Lett.* **82**, 4142–4145 (1999). doi: 10.1103/PhysRevLett.82.4142
9. J.-X. Cheng, L. D. Book, X. S. Xie, Polarization coherent anti-Stokes Raman scattering microscopy. *Opt. Lett.* **26**, 1341–1343 (2001). doi: 10.1364/OL.26.001341; pmid: 18049602
10. J.-X. Cheng, Y. K. Jia, G. Zheng, X. S. Xie, Laser-scanning coherent anti-Stokes Raman scattering microscopy and applications to cell biology. *Biophys. J.* **83**, 502–509 (2002). doi: 10.1016/S0006-3495(02)75186-2; pmid: 12080137
11. A. Volkmer, J.-X. Cheng, X. S. Xie, Vibrational imaging with high sensitivity via epidetected coherent anti-Stokes Raman scattering microscopy. *Phys. Rev. Lett.* **87**, 023901 (2001). doi: 10.1103/PhysRevLett.87.023901
12. C. L. Evans et al., Chemical imaging of tissue in vivo with video-rate coherent anti-Stokes Raman scattering microscopy. *Proc. Natl. Acad. Sci. U.S.A.* **102**, 16807–16812 (2005). doi: 10.1073/pnas.0508282102; pmid: 16263923
13. J.-X. Cheng, X. S. Xie, Theoretical and experimental characterization of coherent anti-Stokes Raman scattering microscopy. *J. Opt. Soc. Am. B* **19**, 1363 (2002). doi: 10.1364/JOSAB.19.001363
14. J.-X. Cheng, A. Volkmer, L. D. Book, X. S. Xie, Multiplex coherent anti-Stokes Raman scattering microspectroscopy and study of lipid vesicles. *J. Phys. Chem. B* **106**, 8493–8498 (2002). doi: 10.1021/jp025771z
15. M. Müller, J. M. Schins, Imaging the thermodynamic state of lipid membranes with multiplex CARS microscopy. *J. Phys. Chem. B* **106**, 3715–3723 (2002). doi: 10.1021/jp014012y
16. T. T. Le, S. Yue, J.-X. Cheng, Shedding new light on lipid biology with coherent anti-Stokes Raman scattering microscopy. *J. Lipid Res.* **51**, 3091–3102 (2010). doi: 10.1194/jlr.R008730; pmid: 20713649
17. E. J. Woodbury, W. K. Ng, Ruby operation in the near IR. *Proc. Inst. Radio Eng.* **50**, 2367 (1962).
18. A. Owyoung, E. D. Jones, Stimulated Raman spectroscopy using low-power cw lasers. *Opt. Lett.* **1**, 152–154 (1977). doi: 10.1364/OL.1.000152; pmid: 19680362

19. E. Ploetz, S. Laimgruber, S. Berner, W. Zinth, P. Gilch, Femtosecond stimulated Raman microscopy. *Appl. Phys. B* **87**, 389–393 (2007). doi: 10.1007/s00340-007-2630-x
20. C. W. Freudiger et al., Label-free biomedical imaging with high sensitivity by stimulated Raman scattering microscopy. *Science* **322**, 1857–1861 (2008). doi: 10.1126/science.1165758; pmid: 19095943
21. Y. Ozeki, F. Dake, S. Kajiyama, K. Fukui, K. Itoh, Analysis and experimental assessment of the sensitivity of stimulated Raman scattering microscopy. *Opt. Express* **17**, 3651–3658 (2009). doi: 10.1364/OE.17.003651; pmid: 19259205
22. P. Nandakumar, A. Kovalev, A. Volkmer, Vibrational imaging based on stimulated Raman scattering microscopy. *New J. Phys.* **11**, 033026 (2009). doi: 10.1088/1367-2630/11/3/033026
23. D. Zhang, M. N. Slipchenko, J.-X. Cheng, Highly sensitive vibrational imaging by femtosecond pulse stimulated Raman loss. *J. Phys. Chem. Lett.* **2**, 1248–1253 (2011). doi: 10.1021/jz200516n; pmid: 21731798
24. E. R. Andresen, P. Berto, H. Rigneault, Stimulated Raman scattering microscopy by spectral focusing and fiber-generated soliton as Stokes pulse. *Opt. Lett.* **36**, 2387–2389 (2011). doi: 10.1364/OL.36.002387; pmid: 21725420
25. H. T. Beier, G. D. Noojin, B. A. Rockwell, Stimulated Raman scattering using a single femtosecond oscillator with flexibility for imaging and spectral applications. *Opt. Express* **19**, 18885–18892 (2011). doi: 10.1364/OE.19.018885; pmid: 21996830
26. M. N. Slipchenko, R. A. Oglesbee, D. Zhang, W. Wu, J.-X. Cheng, Heterodyne detected nonlinear optical imaging in a lock-in free manner. *J. Biophotonics* **5**, 801–807 (2012). doi: 10.1002/jbio.201200005; pmid: 22389310
27. W. Min, C. W. Freudiger, S. Lu, X. S. Xie, Coherent nonlinear optical imaging: Beyond fluorescence microscopy. *Annu. Rev. Phys. Chem.* **62**, 507–530 (2011). doi: 10.1146/annurev.physchem.012809.103512; pmid: 21453061
28. D. Zhang, P. Wang, M. N. Slipchenko, J.-X. Cheng, Fast vibrational imaging of single cells and tissues by stimulated Raman scattering microscopy. *Acc. Chem. Res.* **47**, 2282–2290 (2014). doi: 10.1021/ar400331q; pmid: 24871269
29. A. G. Bell, On the production and reproduction of sound by light. *Am. J. Sci.* **20**, 305–324 (1880). doi: 10.2475/ajs.s3-20.118.305
30. V. Ntziachristos, Going deeper than microscopy: The optical imaging frontier in biology. *Nat. Methods* **7**, 603–614 (2010). doi: 10.1038/nmeth.1483; pmid: 20676081
31. L. V. Wang, S. Hu, Photoacoustic tomography: In vivo imaging from organelles to organs. *Science* **335**, 1458–1462 (2012). doi: 10.1126/science.1216210; pmid: 22442475
32. H.-W. Wang et al., Label-free bond-selective imaging by listening to vibrationally excited molecules. *Phys. Rev. Lett.* **106**, 238106 (2011). doi: 10.1103/PhysRevLett.106.238106; pmid: 21770549
33. V. V. Yakovlev et al., Stimulated Raman photoacoustic imaging. *Proc. Natl. Acad. Sci. U.S.A.* **107**, 20335–20339 (2010). doi: 10.1073/pnas.1012432107; pmid: 21059930
34. H. Wang, Y. Fu, J.-X. Cheng, Experimental observation and theoretical analysis of Raman resonance–enhanced photodamage in coherent anti-Stokes Raman scattering microscopy. *J. Opt. Soc. Am. B* **24**, 544 (2007). doi: 10.1364/JOSAB.24.000544
35. V. V. Yakovlev, G. D. Noojin, M. L. Denton, B. A. Rockwell, R. J. Thomas, Monitoring stimulated Raman scattering with photoacoustic detection. *Opt. Lett.* **36**, 1233–1235 (2011). doi: 10.1364/OL.36.001233; pmid: 21479040
36. P. Wang, J. R. Rajian, J.-X. Cheng, Spectroscopic imaging of deep tissue through photoacoustic detection of molecular vibration. *J. Phys. Chem. Lett.* **4**, 2177–2185 (2013). doi: 10.1021/jz400559a; pmid: 24073304
37. P. Wang et al., High-speed intravascular photoacoustic imaging of lipid-laden atherosclerotic plaque enabled by a 2-kHz barium nitrite raman laser. *Sci. Rep.* **4**, 6889 (2014). doi: 10.1038/srep06889; pmid: 25366991
38. J. R. Rajian, R. Li, P. Wang, J.-X. Cheng, Vibrational photoacoustic tomography: Chemical imaging beyond the ballistic regime. *J. Phys. Chem. Lett.* **4**, 3211–3215 (2013). doi: 10.1021/jz401638e; pmid: 24224071
39. R. Li et al., Assessing breast tumor margin by multispectral photoacoustic tomography. *Biomed. Opt. Express* **6**, 1273–1281 (2015). doi: 10.1364/BOE.6.001273; pmid: 25909011
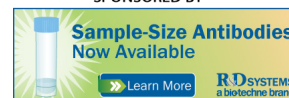
40. R. Li, E. Phillips, P. Wang, C. J. Goergen, J.-X. Cheng, Label-free in vivo imaging of peripheral nerve by multispectral photoacoustic tomography. *J. Biophoton.* 10.1002/jbio.201500004 (2015). doi: 10.1364/BOE.6.001273; pmid: 25909011

41. P. Matousek *et al.*, Subsurface probing in diffusely scattering media using spatially offset Raman spectroscopy. *Appl. Spectrosc.* **59**, 393–400 (2005). doi: 10.1366/0003702053641450; pmid: 15901323

42. M. V. Schulmerich, Noninvasive Raman tomographic imaging of canine bone tissue. *J. Biomed. Opt.* **13**, 020506 (2008). doi: 10.1117/1.2904940; pmid: 18465948

43. A. H. Hielscher *et al.*, Near-infrared diffuse optical tomography. *Dis. Markers* **18**, 313–337 (2002). doi: 10.1155/2002/164252; pmid: 14646043

44. B. G. Saar *et al.*, Video-rate molecular imaging in vivo with stimulated Raman scattering. *Science* **330**, 1368–1370 (2010). doi: 10.1126/science.1197236; pmid: 21127249

45. Y. Ozeki *et al.*, High-speed molecular spectral imaging of tissue with stimulated Raman scattering. *Nat. Photonics* **6**, 845–851 (2012). doi: 10.1038/nphoton.2012.263

46. B. Liu *et al.*, Vibrational fingerprint mapping reveals spatial distribution of functional groups of lignin in plant cell wall. *Anal. Chem.* **87**, 9436–9442 (2015). doi: 10.1021/acs.analchem.5b02434; pmid: 26291845

47. M. Müller, A. Zumbusch, Coherent anti-Stokes Raman scattering microscopy. *ChemPhysChem* **8**, 2156–2170 (2007). doi: 10.1002/cphc.200700202; pmid: 17768730

48. E. M. Vartiainen, H. A. Rinia, M. Müller, M. Bonn, Direct extraction of Raman line-shapes from congested CARS spectra. *Opt. Express* **14**, 3622–3630 (2006). doi: 10.1364/OE.14.003622; pmid: 19516509

49. M. T. Cicerone, K. A. Aamer, Y. J. Lee, E. Vartiainen, Maximum entropy and time-domain Kramers–Kronig phase retrieval approaches are functionally equivalent for CARS microspectroscopy. *J. Raman Spectrosc.* **43**, 637–643 (2012). doi: 10.1002/jrs.3169

50. D. L. Marks, S. A. Boppart, Nonlinear interferometric vibrational imaging. *Phys. Rev. Lett.* **92**, 123905 (2004). doi: 10.1103/PhysRevLett.92.123905; pmid: 15089675

51. C. H. Camp Jr. *et al.*, High-speed coherent Raman fingerprint imaging of biological tissues. *Nat. Photonics* **8**, 627–634 (2014). doi: 10.1038/nphoton.2014.145; pmid: 25621002

52. D. Fu *et al.*, Quantitative chemical imaging with multiplex stimulated Raman scattering microscopy. *J. Am. Chem. Soc.* **134**, 3623–3626 (2012). doi: 10.1021/ja210081h; pmid: 22316340

53. B. Marx, L. Czerwinski, R. Light, M. Somekh, P. Gilch, Multichannel detectors for femtosecond stimulated Raman microscopy–ideal and real ones. *J. Raman Spectrosc.* **45**, 521–527 (2014). doi: 10.1002/jrs.4528

54. W. Rock, M. Bonn, S. H. Parekh, Near shot-noise limited hyperspectral stimulated Raman spectroscopy using low energy lasers and a fast CMOS array. *Opt. Express* **21**, 15113–15120 (2013). doi: 10.1364/OE.21.015113; pmid: 23842298

55. K. Seto, Y. Okuda, E. Tokunaga, T. Kobayashi, Development of a multiplex stimulated Raman microscope for spectral imaging through multi-channel lock-in detection. *Rev. Sci. Instrum.* **84**, 083705 (2013). doi: 10.1063/1.4818670; pmid: 24007071

56. C.-S. Liao *et al.*, Microsecond scale vibrational spectroscopic imaging by multiplex stimulated Raman scattering microscopy. *Light Sci. Appl.* **4**, e265 (2015). doi: 10.1038/lsa.2015.38; pmid: 26167336

57. C.-S. Liao *et al.*, Spectrometer-free vibrational imaging by retrieving stimulated Raman signal from highly scattered photons. *Sci. Advances* **1**, e1500738 (2015). doi: 10.1126/sciadv.1500738

58. D. Fu, G. Holtom, C. Freudiger, X. Zhang, X. S. Xie, Hyperspectral imaging with stimulated Raman scattering by chirped femtosecond lasers. *J. Phys. Chem. B* **117**, 4634–4640 (2013). doi: 10.1021/jp308938t; pmid: 23256635

59. C.-Y. Lin *et al.*, Picosecond spectral coherent anti-Stokes Raman scattering imaging with principal component analysis of meibomian glands. *J. Biomed. Opt.* **16**, 021104 (2011). doi: 10.1117/1.3533716; pmid: 21361667

60. C. Krafft *et al.*, A comparative Raman and CARS imaging study of colon tissue. *J. Biophotonics* **2**, 303–312 (2009). doi: 10.1002/jbio.200810063; pmid: 19434617

61. D. Fu, X. S. Xie, Reliable cell segmentation based on spectral phasor analysis of hyperspectral stimulated Raman scattering imaging data. *Anal. Chem.* **86**, 4115–4119 (2014). doi: 10.1021/ac500014b; pmid: 24684208

62. D. Zhang *et al.*, Quantitative vibrational imaging by hyperspectral stimulated Raman scattering microscopy and multivariate curve resolution analysis. *Anal. Chem.* **85**, 98–106 (2013). doi: 10.1021/ac3019119; pmid: 23198914

63. Y. J. Lee, D. Moon, K. B. Migler, M. T. Cicerone, Quantitative image analysis of broadband CARS hyperspectral images of polymer blends. *Anal. Chem.* **83**, 2733–2739 (2011). doi: 10.1021/ac103351q; pmid: 21395296

64. F. Masia, A. Glen, P. Stephens, P. Borri, W. Langbein, Quantitative chemical imaging and unsupervised analysis using hyperspectral coherent anti-Stokes Raman scattering microscopy. *Anal. Chem.* **85**, 10820–10828 (2013). doi: 10.1021/ac402303g; pmid: 24099603

65. E. O. Potma, X. Xie, Detection of single lipid bilayers with coherent anti-Stokes Raman scattering (CARS) microscopy. *J. Raman Spectrosc.* **34**, 642–650 (2003). doi: 10.1002/jrs.1045

66. J.-X. Cheng, Coherent anti-Stokes Raman scattering microscopy. *Appl. Spectrosc.* **61**, 197–208 (2007). doi: 10.1366/000370207781746044; pmid: 17910784

67. L. Li, H. Wang, J.-X. Cheng, Quantitative coherent anti-Stokes Raman scattering imaging of lipid distribution in coexisting domains. *Biophys. J.* **89**, 3480–3490 (2005). doi: 10.1529/biophysj.105.065607; pmid: 16126824

68. S. Yampolsky *et al.*, Seeing a single molecule vibrate through time-resolved coherent anti-Stokes Raman scattering. *Nat. Photonics* **8**, 650–656 (2014). doi: 10.1038/nphoton.2014.143

69. K. Wang *et al.*, Time-lens based hyperspectral stimulated Raman scattering imaging and quantitative spectral analysis. *J. Biophotonics* **6**, 815–820 (2013). pmid: 23840041

70. C.-S. Liao, J. H. Choi, D. Zhang, S. H. Chan, J.-X. Cheng, Denoising stimulated Raman spectroscopic images by total variation minimization. *J. Phys. Chem. C* **119**, 19397–19403 (2015). doi: 10.1021/acs.jpcc.5b06980

71. H. Yamakoshi *et al.*, Imaging of EdU, an alkyne-tagged cell proliferation probe, by Raman microscopy. *J. Am. Chem. Soc.* **133**, 6102–6105 (2011). doi: 10.1021/ja108404p; pmid: 21443184

72. H. Yamakoshi *et al.*, Alkyne-tag Raman imaging for visualization of mobile small molecules in live cells. *J. Am. Chem. Soc.* **134**, 20681–20689 (2012). doi: 10.1021/ja308529n; pmid: 23198907

73. X. S. Xie, J. Yu, W. Y. Yang, Living cells as test tubes. *Science* **312**, 228–230 (2006). doi: 10.1126/science.1127566; pmid: 16614211

74. L. Wei, Y. Yu, Y. Shen, M. C. Wang, W. Min, Vibrational imaging of newly synthesized proteins in live cells by stimulated Raman scattering microscopy. *Proc. Natl. Acad. Sci. U.S.A.* **110**, 11226–11231 (2013). doi: 10.1073/pnas.1303768110; pmid: 23798434

75. G. Bergner *et al.*, Quantitative detection of C-deuterated drugs by CARS microscopy and Raman microspectroscopy. *Analyst* **136**, 3686–3693 (2011). doi: 10.1039/c0an00956c; pmid: 21785774

76. L. Wei *et al.*, Live-cell imaging of alkyne-tagged small biomolecules by stimulated Raman scattering. *Nat. Methods* **11**, 410–412 (2014). doi: 10.1038/nmeth.2878; pmid: 24584195

77. S. Hong *et al.*, Live-cell stimulated Raman scattering imaging of alkyne-tagged biomolecules. *Angew. Chem. Int. Ed.* **53**, 5827–5831 (2014). doi: 10.1002/anie.201400328; pmid: 24753329

78. H. Kim, G. W. Bryant, S. J. Stranick, Superresolution four-wave mixing microscopy. *Opt. Express* **20**, 6042–6051 (2012). doi: 10.1364/OE.20.006042; pmid: 22418482

79. P. Wang *et al.*, Far-field imaging of non-fluorescent species with subdiffraction resolution. *Nat. Photonics* **7**, 449–453 (2013). doi: 10.1038/nphoton.2013.97; pmid: 24436725

80. L. Gong, H. Wang, Breaking the diffraction limit by saturation in stimulated-Raman-scattering microscopy: A theoretical study. *Phys. Rev. A* **90**, 013818 (2014). doi: 10.1103/PhysRevA.90.013818

81. B. Knoll, F. Keilmann, Near-field probing of vibrational absorption for chemical microscopy. *Nature* **399**, 134–137 (1999). doi: 10.1038/20154

82. H. W. Siesler, Y. Ozaki, S. Kawata, H. M. Heise, *Near-Infrared Spectroscopy: Principles, Instruments, Applications.* (Wiley-VCH, 2002).

83. T. Durduran, R. Choe, W. B. Baker, A. G. Yodh, Diffuse optics for tissue monitoring and tomography. *Rep. Prog. Phys.* **73**, 076701 (2010). doi: 10.1088/0034-4885/73/7/076701; pmid: 26120204

84. N. Everall, T. Hahn, P. Matousek, A. W. Parker, M. Towrie, Picosecond time-resolved Raman spectroscopy of solids: Capabilities and limitations for fluorescence rejection and the influence of diffuse reflectance. *Appl. Spectrosc.* **55**, 1701–1708 (2001). doi: 10.1366/0003702011954053

85. N. Everall, T. Hahn, P. Matousek, A. W. Parker, M. Towrie, Photon migration in Raman spectroscopy. *Appl. Spectrosc.* **58**, 591–597 (2004). doi: 10.1366/000370204774103426; pmid: 15165336

86. M. D. Keller, S. K. Majumder, A. Mahadevan-Jansen, Spatially offset Raman spectroscopy of layered soft tissues. *Opt. Lett.* **34**, 926–928 (2009). doi: 10.1364/OL.34.000926; pmid: 19340173

87. I. E. Iping Petterson, P. Dvořák, J. B. Buijs, C. Gooijer, F. Ariese, Time-resolved spatially offset Raman spectroscopy for depth analysis of diffusely scattering layers. *Analyst* **135**, 3255–3259 (2010). doi: 10.1039/c0an00611d; pmid: 20941438

88. K. A. Esmonde-White, F. W. Esmonde-White, M. D. Morris, B. J. Roessler, Fiber-optic Raman spectroscopy of joint tissues. *Analyst* **136**, 1675–1685 (2011). doi: 10.1039/c0an00824a; pmid: 21359366

89. K. Buckley, J. G. Kerns, A. W. Parker, A. E. Goodship, P. Matousek, Decomposition of in vivo spatially offset Raman spectroscopy data using multivariate analysis techniques. *J. Raman Spectrosc.* **45**, 188–192 (2014). doi: 10.1002/jrs.4434

90. M. V. Schulmerich, W. F. Finney, R. A. Fredricks, M. D. Morris, Subsurface Raman spectroscopy and mapping using a globally illuminated non-confocal fiber-optic array probe in the presence of Raman photon migration. *Appl. Spectrosc.* **60**, 109–114 (2006). doi: 10.1366/000370206776023340; pmid: 16542561

91. S. Srinivasan *et al.*, Image-guided Raman spectroscopic recovery of canine cortical bone contrast in situ. *Opt. Express* **16**, 12190–12200 (2008). doi: 10.1364/OE.16.012190; pmid: 18679495

92. S. Sil, S. Umapathy, Raman spectroscopy explores molecular structural signatures of hidden materials in depth: Universal multiple angle Raman spectroscopy. *Sci. Rep.* **4**, 5308 (2014). doi: 10.1038/srep05308; pmid: 24930768

93. J.-L. H. Demers, F. W. Esmonde-White, K. A. Esmonde-White, M. D. Morris, B. W. Pogue, Next-generation Raman tomography instrument for non-invasive in vivo bone imaging. *Biomed. Opt. Express* **6**, 793–806 (2015). doi: 10.1364/BOE.6.000793; pmid: 25798304

94. T. J. Allen, A. Hall, A. P. Dhillon, J. S. Owen, P. C. Beard, Spectroscopic photoacoustic imaging of lipid-rich plaques in the human aorta in the 740 to 1400 nm wavelength range. *J. Biomed. Opt.* **17**, 061209 (2012). doi: 10.1117/1.JBO.17.6.061209; pmid: 22734739

95. K. Jansen, A. F. W. van der Steen, H. M. M. van Beusekom, J. W. Oosterhuis, G. van Soest, Intravascular photoacoustic imaging of human coronary atherosclerosis. *Opt. Lett.* **36**, 597–599 (2011). doi: 10.1364/OL.36.000597; pmid: 21368919

96. P. Wang, P. Wang, H.-W. Wang, J.-X. Cheng, Mapping lipid and collagen by multispectral photoacoustic imaging of chemical bond vibration. *J. Biomed. Opt.* **17**, 96010–96011 (2012). pmid: 23085911

97. K. Jansen, M. Wu, A. F. van der Steen, G. van Soest, Photoacoustic imaging of human coronary atherosclerosis in two spectral bands. *Photoacoustics* **2**, 12–20 (2014). doi: 10.1016/j.pacs.2013.11.003; pmid: 25302152

98. P. Wang, H.-W. Wang, M. Sturek, J.-X. Cheng, Bond-selective imaging of deep tissue through the optical window between 1600 and 1850 nm. *J. Biophotonics* **5**, 25–32 (2012). doi: 10.1002/jbio.201100102; pmid: 22125288

99. B. G. Saar *et al.*, Label-free, real-time monitoring of biomass processing with stimulated Raman scattering microscopy. *Angew. Chem. Int. Ed.* **49**, 5476–5479 (2010). doi: 10.1002/anie.201000900; pmid: 20589818

100. J. C. Mansfield *et al.*, Label-free chemically specific imaging in planta with stimulated Raman scattering microscopy. *Anal. Chem.* **85**, 5055–5063 (2013). doi: 10.1021/ac400266a; pmid: 23581493

101. X. Nan, J.-X. Cheng, X. S. Xie, Vibrational imaging of lipid droplets in live fibroblast cells with coherent anti-Stokes Raman scattering microscopy. *J. Lipid Res.* **44**, 2202–2208 (2003). doi: 10.1194/jlr.D300022-JLR200; pmid: 12923234

102. T. Hellerer *et al.*, Monitoring of lipid storage in *Caenorhabditis elegans* using coherent anti-Stokes Raman scattering (CARS) microscopy. *Proc. Natl. Acad. Sci. U.S.A.* **104**, 14658–14663 (2007). doi: 10.1073/pnas.0703594104; pmid: 17804796

103. R. K. Lyn, D. C. Kennedy, A. Stolow, A. Ridsdale, J. P. Pezacki, Dynamics of lipid droplets induced by the hepatitis C virus

core protein. *Biochem. Biophys. Res. Commun.* **399**, 518–524 (2010). doi: 10.1016/j.bbrc.2010.07.101; pmid: 20678475

104. J. P. Day, G. Rago, K. F. Domke, K. P. Velikov, M. Bonn, Label-free imaging of lipophilic bioactive molecules during lipid digestion by multiplex coherent anti-Stokes Raman scattering microspectroscopy. *J. Am. Chem. Soc.* **132**, 8433–8439 (2010). doi: 10.1021/ja102069d; pmid: 20507119

105. M. Paar *et al.*, Remodeling of lipid droplets during lipolysis and growth in adipocytes. *J. Biol. Chem.* **287**, 11164–11173 (2012). doi: 10.1074/jbc.M111.316794; pmid: 22311986

106. M. C. Wang, W. Min, C. W. Freudiger, G. Ruvkun, X. S. Xie, RNAi screening for fat regulatory genes with SRS microscopy. *Nat. Methods* **8**, 135–138 (2011). doi: 10.1038/nmeth.1556; pmid: 21240281

107. W. Dou, D. Zhang, Y. Jung, J.-X. Cheng, D. M. Umulis, Label-free imaging of lipid-droplet intracellular motion in early *Drosophila* embryos using femtosecond-stimulated Raman loss microscopy. *Biophys. J.* **102**, 1666–1675 (2012). doi: 10.1016/j.bpj.2012.01.057; pmid: 22500767

108. P. Wang *et al.*, Imaging lipid metabolism in live *Caenorhabditis elegans* using fingerprint vibrations. *Angew. Chem. Int. Ed.* **53**, 11787–11792 (2014). doi: 10.1002/anie.201406029; pmid: 25195517

109. M. N. Slipchenko, T. T. Le, H. Chen, J.-X. Cheng, High-speed vibrational imaging and spectral analysis of lipid bodies by compound Raman microscopy. *J. Phys. Chem. B* **113**, 7681–7686 (2009). doi: 10.1021/jp902231y; pmid: 19422201

110. S. Yue *et al.*, Cholesteryl ester accumulation induced by PTEN loss and PI3K/AKT activation underlies human prostate cancer aggressiveness. *Cell Metab.* **19**, 393–406 (2014). doi: 10.1016/j.cmet.2014.01.019; pmid: 24606897

111. H. Wang, Y. Fu, P. Zickmund, R. Shi, J.-X. Cheng, Coherent anti-stokes Raman scattering imaging of axonal myelin in live spinal tissues. *Biophys. J.* **89**, 581–591 (2005). doi: 10.1529/biophysj.105.061911; pmid: 15834003

112. Y. Fu, H. Wang, T. B. Huff, R. Shi, J. X. Cheng, Coherent anti-Stokes Raman scattering imaging of myelin degradation reveals a calcium-dependent pathway in lyso-PtdCho-induced demyelination. *J. Neurosci. Res.* **85**, 2870–2881 (2007). doi: 10.1002/jnr.21403; pmid: 17551984

113. Y. Shi *et al.*, Longitudinal in vivo coherent anti-Stokes Raman scattering imaging of demyelination and remyelination in injured spinal cord. *J. Biomed. Opt.* **16**, 106012 (2011). doi: 10.1117/1.3641988; pmid: 22029359

114. E. Bélanger *et al.*, In vivo evaluation of demyelination and remyelination in a nerve crush injury model. *Biomed. Opt. Express* **2**, 2698–2708 (2011). doi: 10.1364/BOE.2.002698; pmid: 22091449

115. C.-R. Hu, D. Zhang, M. N. Slipchenko, J.-X. Cheng, B. Hu, Label-free real-time imaging of myelination in the *Xenopus laevis* tadpole by in vivo stimulated Raman scattering microscopy. *J. Biomed. Opt.* **19**, 086005 (2014). doi: 10.1117/1.JBO.19.8.086005; pmid: 25104411

116. Y. Shen, F. Xu, L. Wei, F. Hu, W. Min, Live-cell quantitative imaging of proteome degradation by stimulated Raman scattering. *Angew. Chem. Int. Ed.* **53**, 5596–5599 (2014). doi: 10.1002/anie.201310725; pmid: 24737659

117. J. Li, J.-X. Cheng, Direct visualization of de novo lipogenesis in single living cells. *Sci. Rep.* **4**, 6807 (2014). doi: 10.1038/srep06807; pmid: 25351207

118. F. Hu, L. Wei, C. Zheng, Y. Shen, W. Min, Live-cell vibrational imaging of choline metabolites by stimulated Raman scattering coupled with isotope-based metabolic labeling. *Analyst* **139**, 2312–2317 (2014). doi: 10.1039/c3an02281a; pmid: 24555181

119. H. J. Lee *et al.*, Assessing cholesterol storage in live cells and *C. elegans* by stimulated Raman scattering imaging of

phenyl-Diyne cholesterol. *Sci. Rep.* **5**, 7930 (2015). doi: 10.1038/srep07930; pmid: 25608867

120. A. Pliss, A. N. Kuzmin, A. V. Kachynski, P. N. Prasad, Biophotonic probing of macromolecular transformations during apoptosis. *Proc. Natl. Acad. Sci. U.S.A.* **107**, 12771–12776 (2010). doi: 10.1073/pnas.1006374107; pmid: 20615987

121. F.-K. Lu *et al.*, Label-free DNA imaging in vivo with stimulated Raman scattering microscopy. *Proc. Natl. Acad. Sci. U.S.A.* **112**, 11624–11629 (2015). doi: 10.1073/pnas.1515121112; pmid: 26324899

122. E. Kang *et al.*, In situ visualization of paclitaxel distribution and release by coherent anti-Stokes Raman scattering microscopy. *Anal. Chem.* **78**, 8036–8043 (2006). doi: 10.1021/ac061218s; pmid: 17134137

123. M. N. Slipchenko *et al.*, Vibrational imaging of tablets by epi-detected stimulated Raman scattering microscopy. *Analyst* **135**, 2613–2619 (2010). doi: 10.1039/c0an00252f; pmid: 20625604

124. C. M. Hartshorn *et al.*, Multicomponent chemical imaging of pharmaceutical solid dosage forms with broadband CARS microscopy. *Anal. Chem.* **85**, 8102–8111 (2013). doi: 10.1021/ac400671p; pmid: 23855585

125. A. L. Fussell, F. Grasmeijer, H. W. Frijlink, A. H. de Boer, H. L. Offerhaus, CARS microscopy as a tool for studying the distribution of micronised drugs in adhesive mixtures for inhalation. *J. Raman Spectrosc.* **45**, 495–500 (2014). doi: 10.1002/jrs.4515

126. W. S. Chiu *et al.*, Molecular diffusion in the human nail measured by stimulated Raman scattering microscopy. *Proc. Natl. Acad. Sci. U.S.A.* **112**, 7725–7730 (2015). doi: 10.1073/pnas.1503791112; pmid: 26056283

127. D. Fu *et al.*, Imaging the intracellular distribution of tyrosine kinase inhibitors in living cells with quantitative hyperspectral stimulated Raman scattering. *Nat. Chem.* **6**, 614–622 (2014). doi: 10.1038/nchem.1961; pmid: 24950332

128. S. Yue, M. N. Slipchenko, J.-X. Cheng, Multimodal nonlinear optical microscopy. *Laser Photon. Rev.* **5**, 496–512 (2011). doi: 10.1002/lpor.201000027; pmid: 24353747

129. C. W. Freudiger *et al.*, Multicolored stain-free histopathology with coherent Raman imaging. *Lab. Invest.* **92**, 1492–1502 (2012). doi: 10.1038/labinvest.2012.109; pmid: 22906986

130. F. Légaré, C. L. Evans, F. Ganikhanov, X. S. Xie, Towards CARS endoscopy. *Opt. Express* **14**, 4427–4432 (2006). doi: 10.1364/OE.14.004427; pmid: 19516594

131. B. G. Saar, R. S. Johnston, C. W. Freudiger, X. S. Xie, E. J. Seibel, Coherent Raman scanning fiber endoscopy. *Opt. Lett.* **36**, 2396–2398 (2011). doi: 10.1364/OL.36.002396; pmid: 21725423

132. Z. Liu *et al.*, Development of fibre bundle probe for coherent anti-Stokes Raman scattering microendoscopy. *Electron. Lett.* **49**, 522 (2013). doi: 10.1049/el.2013.0220

133. S. Heuke *et al.*, Multimodal mapping of human skin. *Br. J. Dermatol.* **169**, 794–803 (2013). pmid: 23927013

134. K. König *et al.*, Optical skin biopsies by clinical CARS and multiphoton fluorescence/SHG tomography. *Laser Phys. Lett.* **8**, 465–468 (2011). doi: 10.1002/lapl.201110014

135. M. Weinigel *et al.*, In vivo histology: Optical biopsies with chemical contrast using clinical multiphoton/coherent anti-Stokes Raman scattering tomography. *Laser Phys. Lett.* **11**, 055601 (2014). doi: 10.1088/1612-2011/11/5/055601

136. R. Mittal *et al.*, Evaluation of stimulated Raman scattering microscopy for identifying squamous cell carcinoma in human skin. *Lasers Surg. Med.* **45**, 496–502 (2013). pmid: 23996592

137. M. Ji *et al.*, Rapid, label-free detection of brain tumors with stimulated Raman scattering microscopy. *Sci. Transl. Med.* **5**, 201ra119 (2013). doi: 10.1126/scitranslmed.3005954; pmid: 24005159

138. M. Jermyn *et al.*, Intraoperative brain cancer detection with Raman spectroscopy in humans. *Sci. Transl. Med.* **7**, 274ra19 (2015). doi: 10.1126/scitranslmed.aaa2384; pmid: 25673764

139. B. Wang *et al.*, Intravascular photoacoustic imaging of lipid in atherosclerotic plaques in the presence of luminal blood. *Opt. Lett.* **37**, 1244–1246 (2012). doi: 10.1364/OL.37.001244; pmid: 22466209

140. R. Li, M. N. Slipchenko, P. Wang, J.-X. Cheng, Compact high power barium nitrite crystal-based Raman laser at 1197 nm for photoacoustic imaging of fat. *J. Biomed. Opt.* **18**, 040502 (2013). doi: 10.1117/1.JBO.18.4.040502; pmid: 23536057

141. A. Cerussi *et al.*, In vivo absorption, scattering, and physiologic properties of 58 malignant breast tumors determined by broadband diffuse optical spectroscopy. *J. Biomed. Opt.* **11**, 044005 (2006). doi: 10.1117/1.2337546; pmid: 16965162

142. S. Kukreti, A. Cerussi, B. Tromberg, E. Gratton, Intrinsic near-infrared spectroscopic markers of breast tumors. *Dis. Markers* **25**, 281–290 (2008). doi: 10.1155/2008/651308; pmid: 19208946

143. A. E. Cerussi *et al.*, Diffuse optical spectroscopic imaging correlates with final pathological response in breast cancer neoadjuvant chemotherapy. *Phil. Trans. R. Soc. A* **369**, 4512–4530 (2011). doi: 10.1098/rsta.2011.0279; pmid: 22006904

144. N. Stone, R. Baker, K. Rogers, A. W. Parker, P. Matousek, Subsurface probing of calcifications with spatially offset Raman spectroscopy (SORS): Future possibilities for the diagnosis of breast cancer. *Analyst* **132**, 899–905 (2007). doi: 10.1039/b705029a; pmid: 17710265

145. M. V. Schulmerich, K. A. Dooley, T. M. Vanasse, S. A. Goldstein, M. D. Morris, Subsurface and transcutaneous Raman spectroscopy and mapping using concentric illumination rings and collection with a circular fiber-optic array. *Appl. Spectrosc.* **61**, 671–678 (2007). doi: 10.1366/000370207781393307; pmid: 17697459

146. P. Matousek, N. Stone, Recent advances in the development of Raman spectroscopy for deep non-invasive medical diagnosis. *J. Biophotonics* **6**, 7–19 (2013). doi: 10.1002/jbio.201200141; pmid: 23129567

147. I. Rajapaksa, H. Kumar Wickramasinghe, Raman spectroscopy and microscopy based on mechanical force detection. *Appl. Phys. Lett.* **99**, 161103–1611033 (2011). doi: 10.1063/1.3652760; pmid: 22087048

148. X. Xu, H. Liu, L. V. Wang, Time-reversed ultrasonically encoded optical focusing into scattering media. *Nat. Photonics* **5**, 154–157 (2011). doi: 10.1038/nphoton.2010.306; pmid: 21532925

149. Y. M. Wang, B. Judkewitz, C. A. Dimarzio, C. Yang, Deep-tissue focal fluorescence imaging with digitally time-reversed ultrasound-encoded light. *Nat. Commun.* **3**, 928 (2012). doi: 10.1038/ncomms1925; pmid: 22735456

150. C. W. Freudiger *et al.*, Stimulated Raman scattering microscopy with a robust fibre laser source. *Nat. Photonics* **8**, 153–159 (2014). doi: 10.1038/nphoton.2013.360; pmid: 25313312

ACKNOWLEDGMENTS